Energy & Environmental Science

ROYAL SOCIETY
OF CHEMISTRY

PAPER
Thibaut Jousseaume, Samuel Tardif *et al*.
Strain and collapse during lithiation of layered transition
metal oxides: a unified picture

PAPER

Strain and collapse during lithiation of layered transition metal oxides: a unified picture†

Thibaut Jousseaume, [a] Jean-François Colin,[b] Marion Chandesris, [b] Sandrine Lyonnard[a] and Samuel Tardif *[a]

Developing long-life, high-energy density materials such as the Ni-rich $LiNi_xMn_yCo_zO_2$ (NMC*xyz*) is needed to manufacture advanced Li-ion batteries. However, these compounds suffer from a capacity fade upon cycling, attributed to the H2–H3 phase transition and to the associated volume changes. Here, by applying *operando* XRD we show that the usually blamed H2-H3 transition is actually not taking place in Ni-rich layered transition metal oxides, except for the 100% nickel composition LNO. We find a universal mechanism instead, that only depends on the lithium content, irrespective of nickel content, applied charge rate or phase diagram of the bulk material. We discover that strain appears when the structure collapses, below 40% lithium in the layers. Below this critical lithium content, exponentially growing strain and large lattice distortions occur, which may favor irreversible cracks. Since lithium loss upon cycling induces a shift towards lower lithium content in positive active material, the consequences of repeated and irreversible stress are expected to be exacerbated on the long-term. Therefore, unifying structure, crystalline strain and cracks, our results reveal that the lithium content window is the main driver of degradation in layered transition metal oxides, rather than the potential window.

Broader context

The automotive industry aims at improving the performance of electric batteries in terms of fast charging, stored energy capacity and lifetime to meet the needs of their customers. Layered transition metal (TM) oxides such as $LiNi_xMn_yCo_zO_2$ (NMC*xyz*) with high nickel content (Ni-rich) have a better energy density than those with medium nickel content. However, they exhibit accelerated capacity loss during cycling, which limits their use. In this paper we identify the cause of the larger degradation of Ni-rich NMCs compared to their Ni-poor counterparts. The identification of this mechanism was made possible by unifying the lithium intercalation mechanism of various Ni-rich NMCs under different kinetic conditions. Based on this mechanism, we show that these degradation are indeed common to all layered TM oxides, and that they escalate in the case of Ni-rich NMCs due to the chemical destabilisation of the material when it is lithium depleted during the charge. When the material has a low lithium concentration indeed, it suffers from heterogeneous distortion of the crystalline structure, leading to the appearance of stresses and cracks in the crystals. Hence, we show that lithium loss triggers a variety of degradations in layered TM oxides.

1 Introduction

Current Li-ion battery materials provide moderate energy densities. This remains an issue for electrical mobility applications, where the tremendous characteristics of oil must be surpassed.[1] Increasing the nickel content x in the widely known layered transition metal (TM) oxides $LiNi_xMn_yCo_zO_2$ (NMC*xyz*) can improve the battery capacity, for instance from $LiNi_{0.6}Mn_{0.2}Co_{0.2}O_2$ (NMC622), to $LiNi_{0.8}Mn_{0.1}Co_{0.1}O_2$ (NMC811), and even to 100% of nickel with $LiNiO_2$ (LNO). Indeed, more lithium can be extracted in the electrochemical stability window of carbonate electrolytes when the nickel content is higher. Nevertheless, high nickel content NMCs present a reduced lifetime, which has been ascribed to particle cracks, surface reconstruction, oxygen leaks or heterogeneous behaviour.[2–6] Knowing how to limit these deleterious effects is thus key to develop long lifetime batteries.

The very (de)lithiation mechanism in the NMC materials is still debated in the literature. Contradictory conclusions hinder the elucidation of the fading mechanism, which can be material-dependent. Often, a discontinuous lattice parameter

[a] *Univ. Grenoble Alpes, CEA IRIG, 17 Av. des Martyrs, 38000 Grenoble, France.*
  E-mail: samuel.tardif@cea.fr
[b] *Univ. Grenoble Alpes, CEA LITEN, 17 Av. des Martyrs, 38000 Grenoble, France*
† Electronic supplementary information (ESI) available. See DOI: https://doi.org/10.1039/d3ee04115h

This journal is © The Royal Society of Chemistry 2024

Energy Environ. Sci., 2024, **17**, 2753–2764 | **2753**

evolution was reported for Ni-rich NMC, with three hexagonal phases H1, H2 and H3 in charge, characterised by the lattice parameter c as $c_{H2} > c_{H1} > c_{H3}$.[7–12] However, other studies found a continuous lattice parameter evolution, that describes the material with a single hexagonal structure all along the process, after the first delithiation.[13–16] Moreover, the effect of the nickel content on the lithiation mechanism is not entirely grasped as well. For instance, Ryu *et al.*[3] reported that NMCs with 90% and 95% nickel content undergo a phase transformation, whereas 60% and 80% nickel contents do not, in contrast with the single phase mechanism proposed by Li *et al.*[17] in NMC from 30% to 90% nickel content.

Such differences could be due to errors in the determination of the structural evolution that can stem from several factors: the experimental setup that is used, the cell dedicated to the measurement, or the technique itself. For example, coin cells with a polyimide window, such as the one used by Ryu *et al.*,[3] are reported to have a reaction rate under the window that is slower than elsewhere in the cell.[18] Several other experimental conditions could influence the miscellaneous results mentioned above, such as defects in the material, cell pressure, low angular resolution, separator, cycling potential window, electrode characteristics, or choice of electrolyte.[9,19–21] In addition, the applied charge rate (C-rate) is often study-dependent, but its effect on the material is usually ignored, even though it is bound to the chemical potential.[22] For instance, it has been shown that new thermodynamically metastable phases appear when the charge rate is increased because their nucleation energy is reached.[23] Recently, Wu *et al.*[24] reported the same structural evolution of NMC622 at different C-rates, but with a non-standard electrolyte, and with lower resolution of transfer momentum than standard X-ray diffraction. Since the NMC phase diagram is reported to be influenced by the C-rate,[25] a detailed study of the lithiation mechanism accounting for the charge rate is needed, in representative conditions and with high angular resolution to distinguish phase transformation from heterogeneities that are known to take place in NMC electrodes, especially in large cells.[26–28]

Here, the crystalline structure of several Ni-rich NMCs is investigated using both laboratory and high resolution synchrotron *operando* X-ray diffraction under varied C-rate conditions to evidence the effects of nickel content and applied current on the lithiation. We propose a unified structural model of Ni-rich layered oxides based on the correlated observation and quantification of lattice parameters and strain evolutions during lithiation. This universal model introduces a critical lithium content controlling the evolution of crystalline strain in the materials, and establishes the general conditions for materials irreversible damages on long-term cycling. The key role of lithium loss in battery aging is underlined, suggesting an identical degradation process for layered TM oxides.

2 Materials and method

2.1 Materials

We investigated NMC622, NMC811 and LNO in full cell in single layer format pouch cells. The NMC622 and NMC811 positive electrodes were manufactured at LITEN (Univ. Grenoble Alpes, CEA). The slurry was made of 96% respective active material (Targay), 2.5% polymer binder (PVDF5130, Solvay), and 1.5% additive conductor (1% of Super C65, Imerys and 0.5% of VGCF, Showa Denko), in mass ratio. Those electrodes were stacked with negative electrodes, manufactured at LITEN with a slurry composed of 95% of graphite (Imerys), 2% of thickener (CMC, Ashland), and 3% of binder (SBR, BASF) in mass ratio, coated on a 10 μm-thick copper foil. The LNO electrodes were provided by BASF and composed of 94% of active material, 3% of polymer binder (PVDF5130, Solvay), and 3% of additive conductor (C65 Carbon black, TIMCAL) in mass ratio. The LNO electrode was stacked with the following negative electrode provided by BASF: a 10 μm copper foil coated by 94% of graphite (Imerys), 2% of thickener (CMC, Dow), and 4% additives conductor (2% C45 Carbon black, Imerys and 2% SBR, Zeon). The loadings were 12 and 10.4 mg cm^{-2} respectively for NMC622 and NMC811 electrodes balanced with 7 mg cm^{-2} graphite anodes, and about 4.4 mg cm^{-2} for LNO electrodes on a 20 μm-thick aluminium foil balanced with 3.5 mg cm^{-2} graphite anodes. The electrodes were assembled with a 25 μm-thick separator (Celgard), and sealed in pouch cells in water free (<1 ppm) argon atmosphere. The surface of the positive and negative electrodes are respectively 10.24 cm^2 and 12.25 cm^2. The electrolyte was 1 M LiPF$_6$ in ethylene carbonate (EC), propylene carbonate (PC) and dimethyl carbonate (DMC) in 1:1:3 volume ratio.

2.2 Electrochemical cycling

Each pouch cell was subjected to conditioning cycles at 45 °C before being probed by the synchrotron X-ray beam. The conditioning cycles followed: 5 min at C/20 (C/n is the current needed to charge the cell in n hours), a 12 hours rest period, 4 hours of charge at C/20, ~8 hours at C/10, two discharges and one charge at C/10, and finally a storage at state of charge (SOC) 10% before being measured. During the *operando* X-ray diffraction measurement (XRD), a VSP potentiostat (Biologic) monitored the cell cycling under room temperature (20 ± 2 °C) in galvanostatic conditions. The same cycling protocol was used for the pouch cells measured between C/5 and 2C: charge at C/n until 4.2 V with a voltage hold until the current reaches C/200 or after 1 h 30 min of hold. The discharges were performed at C/n from 4.2 V to 2.5 V with a voltage hold at 2.5 V with the same charge ending conditions.

2.3 *Operando* laboratory X-ray diffraction

Operando laboratory X-ray diffraction (L-XRD) was performed in a Bruker D8 advance diffractometer with a Cu anticathode to follow the slow charge, *i.e.* without kinetic limitations. The active materials were the same as for the pouch cells. They were milled with carbon black in 70:30 mass ratios in a water-free (<0.5 ppm) and oxygen-free (<2 ppm) atmosphere. The mixture was then measured during its first charge in the Leriche cell[29] mounted in half cell configuration with LP100 electrolyte (1 M LiPF$_6$ in EC:PC:DMC in 1:1:3 ratios). The diffraction patterns were recorded in reflection geometry (Bragg–Brentano), using a

2754 | *Energy Environ. Sci.*, 2024, **17**, 2753–2764

This journal is © The Royal Society of Chemistry 2024

beryllium window as a current collector. The XRD patterns were measured *operando* in the $[15°, 79°]$ range as the cell was charged at C/100, each pattern required about 1 h of measurement. The same setup was used to collect diffraction patterns of pristine NMC622 and NMC811. LNO pristine diffraction pattern was measured with the setup used for higher charge rates (see following). The pristine patterns were analysed with the FullProf package to perform the full Rietveld refinement.[30]

2.4 *Operando* synchrotron X-ray diffraction

To study the impact of C-rate, better time resolution was obtained using *operando* synchrotron X-ray diffraction (S-XRD) on BM32 beamline at the European synchrotron radiation facility. The X-ray beam energy was set to 27 keV, and had a size of about 550 μm × 150 μm and a flux of about 5×10^{10} ph s^{-1}. The pouch cells were measured with the setup shown in Fig. 1 in transmission geometry (Debye–Scherrer).

To ensure reproducible conditions, two silicon windows on both sides of the cell applied the pressure homogeneously, in particular at the measurement points. The pouch cells and the silicon windows were held together using a bespoke sample holder, which was tightened with a torque wrench to a constant nominal value. The diffraction patterns were calibrated and integrated from images recorded by a moveable 2D CdTe detector with the use of the pyFAI-multigeometry module.[31] This setup enabled a good angular resolution (7.8×10^{-3}) over the 2θ range $[2°, 30°]$, an adapted temporal resolution of 1 min 30 s for fast charge, and high statistics. Le Bail refinement was applied to every full patterns measured in *operando* conditions,

including L-XRD measurements, to allow high precision in the structure solving using the software Jana2006.[32] The same procedure was applied to partial patterns to allow fast and accurate refinement. Whether analysing the L-XRD or S-XRD data, the anisotropic strain along $[001]$ is fitted when it does not vanish.

3 Results and discussion

3.1 Pristine materials characterisation

Scanning electron microscopy (SEM) images of NMC622, NMC811 and LNO pristine powders in Fig. 2A–C, reveal comparable particle morphologies. Despite distinct nickel contents, they all present primary particle size of 100 nm–1 μm, and secondary particle size of around ten microns (ESI† Section S1). They also share an identical atomic arrangement, as evidenced by Rietveld refinements of the pristine materials indexed on the $R\bar{3}m$ hexagonal space group (Fig. 2D and E). The refined parameters in Table 1 indicate that the higher nickel content is, the lower the c and the higher the a parameters are. Therefore, despite minor differences in lattice parameters, the three materials are very alike at the pristine state.
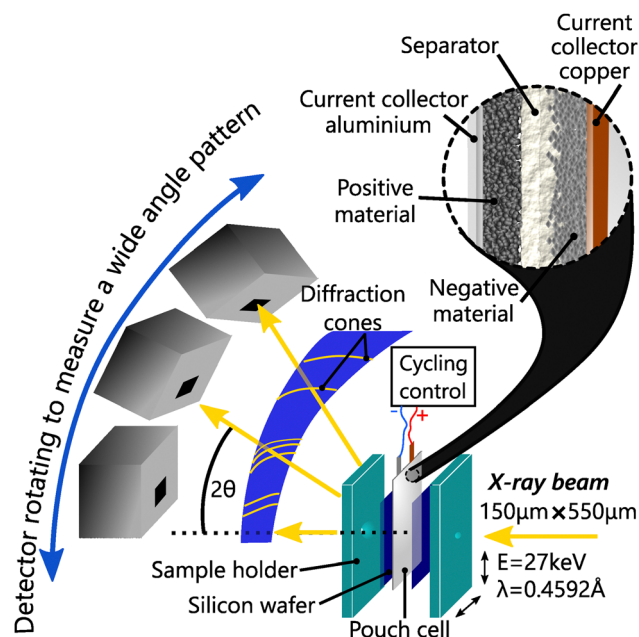

Fig. 1 *Operando* diffraction experiment on pouch cells at BM32 beamline at ESRF. The two faces of the sample holder are screwed with a torque wrench to apply the same pressure to each cell. The cells are inserted between the two faces with silicon wafer on both sides to keep homogeneous pressure at the measurement points.
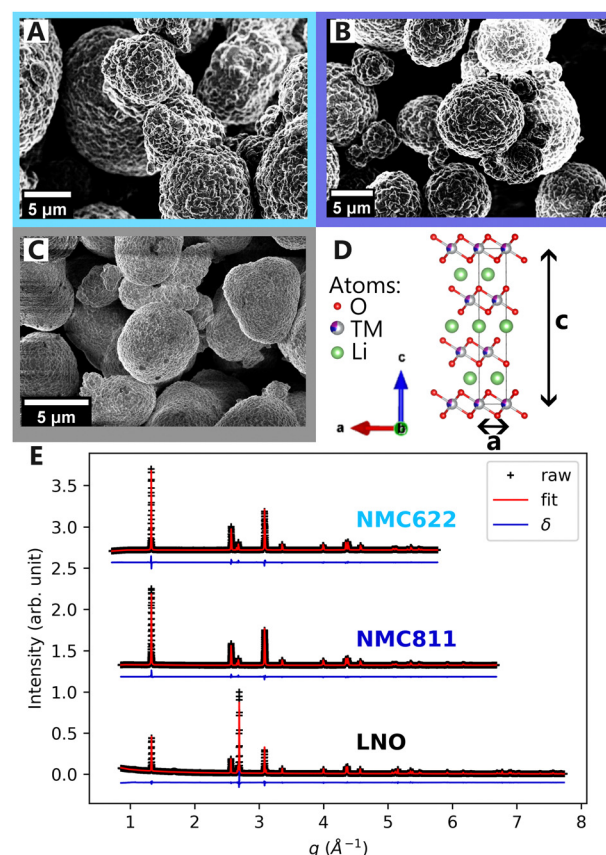

Fig. 2 Structure and morphology of layered powders. SEM images of (A) NMC622, (B) NMC811 and (C) LNO powder. (D) Common unit cell of the three materials with different a and c lattice parameters. (E) Raw XRD patterns, Rietveld refinements and their residuals δ of the three materials. XRD patterns are y-shifted for convenience.

This journal is © The Royal Society of Chemistry 2024

Energy Environ. Sci., 2024, **17**, 2753–2764 | **2755**

3.2 Structural characterisation close to thermodynamic equilibrium

According to the current knowledge, the structure of NMCxyz depends on the nickel content x, the voltage V and the C-rate C_r, and so does the strain. Then, if (f,g) are functions giving respectively the structure X and the strain ε of NMC xyz, then $X = f(x,V,C_r)$ and $\varepsilon = g(x,V,C_r)$. We will progressively show in this article that structure and strain can be simplified as functions of one variable only, the lithium content, featuring the unified structural model. The delithiation of NMC622, NMC811 and LNO was first investigated at very slow charge rate to picture the mechanism close to thermodynamic equilibrium. To this end, *operando* X-ray diffraction in a laboratory diffractometer (L-XRD) was performed using the Leriche cell.[29] *Operando* XRD is particularly suited to characterise time-resolved phase transitions in crystalline materials as it betrays the presence of a phase at a given moment. A change in the structure is reflected by a change in the number, positions or shape of the peaks, making it possible to monitor the evolution of the structure. Here, the 003 and 101 diffraction peaks of NMC622 and NMC811 (Fig. S2A and B respectively, ESI†) are shifting continuously, whereas those of LNO are splitting or shifting discontinuously, indicating a delithiation mechanism of NMC622 and NMC811 different from LNO. Le Bail refinements confirm that LNO is transforming into four different phases through three phase transformations (Fig. 3C and D) as reported in other studies,[33–35] whereas NMC622 and NMC811 are following a solid-solution mechanism (Fig. 3A and B).

Interestingly, we observe that all peaks broaden at the beginning of the charge, while at the end of charge the broadening is specific to the $\langle 00l \rangle$ peaks (Fig. S3D, ESI)†. This effect deserves a detailed analysis, as peak broadening generally carries key additional information on crystalline materials organisation. Indeed as we show in ESI† Section S3, we were able to model the recorded broadenings using the hypothesis of a 1st order phase transition. However as we will extensively discuss in the following sections, it can also be interpreted with a more convincing scenario using a different structural framework, that is a single-phase solid-solution mechanism featuring anisotropic strain.

3.3 Charge rate impact

The impact of charge rate on the delithiation mechanisms was investigated by synchrotron XRD (S-XRD) using pouch cells cycled from C/5 to 2C between 2.5 V and 4.2 V in full cell configuration. A special attention was granted to the setup to be as non-intrusive as possible (Fig. 1). We also reduced the dose absorbed by raster scanning the cells during the cycling and by using a moderate photon flux to limit beam damage in the electrodes. It is necessary to consider it when analysing the impact of C-rate on the phase diagram since beam damage is reported to trigger artificial phase transitions in batteries.[36] In the following, the structure evolution of the material is measured as function of the lithium content c_{Li}. Note that c_{Li} is only obtained from electrochemical data, and does not assume any theoretical value of capacity (see ESI† Section S4).

The startling match of lattice parameters evolution as a function of c_{Li} (Fig. 4) shows that the structural behaviour of the three nickel stoichiometries is not influenced by the applied C-rate. The data recorded before the constant current steps (Fig. S8, ESI†), and the full pattern ('FP') refinement procedure confirm it. The biphasic boundaries of LNO phase transformations are not significantly affected neither. Indeed, the expected enlarging of biphasic zones due to the increase of heterogeneous lithiation states caused by the diffusion hindrance is only measured for the H1 → M transition (Fig. 4C), in the limits of the analysis performed here, and cannot be extended to every transitions. Note that the technique employed here averages the material structure over the electrode depth. The use of S-XRD on a single crystal with a micro beam is needed to elucidate whether C-rate affects the two phases coexistence at the crystal scale in LNO, which is beyond the scope of this work. The structure evolution at C/100 is nearly identical (Fig. S5, ESI†), but with a shift in c_{Li} due to a biased estimation of the lithium content in the *in situ* cell as mentioned in ESI† Section S5. As a result, the structural evolution of the three materials under charge is not changed across at least two orders of magnitude of C-rates. At this point we can write that the structure X is given by $X = f(x,V)$.

3.4 Nickel content effect

We find that the structural behaviour of NMC622, NMC811 and LNO during charge and discharge can be described using a common framework of typical atomic distances rather than the standard crystallographic classification based on specific crystalline lattices and symmetries. Indeed, we only need the distance between neighbouring TM atoms d_{TM} and the inter-layer (IL) distance d_{IL} to build a single structural model accounting for the evolutions of the various materials (Fig. 5A and Fig. S13A, ESI†). This finding is strongly supported by characteristic features common to the NMCs calculated with the derivatives of d_{IL} and d_{TM} vs. c_{Li}. Note that the derivatives of LNO's parameters are discontinuous because 1st order phase transitions are inherently discontinuous. Three key lithium contents can be highlighted (Fig. 5B). (1) A same c_{Li} value of 0.4 where the two NMCs and LNO reach their maximum of d_{IL}. The existence of d_{IL} maximum is related to the competition between the O–O repulsion and the structure collapse. According to the literature, the structure collapse origin could be related to more covalent Ni–O bonds, as evidenced from the decreasing Ni–O distance,[16,34] which in turn weakens the repulsion of neighbouring O layers.[35] (2) No matter the materials, the plateau value of d_{TM} is at $c_{Li} \simeq 0.32$; and (3) the

Table 1 Unit cell description of pristine materials. "$d_{TM–O}$" stands for the distance between transition metal (TM) and oxygen atoms

	NMC622	NMC811	LNO
Space group	$R\bar{3}m$	$R\bar{3}m$	$R\bar{3}m$
a	2.8703	2.8727	2.8747
c	14.2255	14.2127	14.1775
$d_{TM–O}$	1.9732	1.9708	1.9719

2756 | *Energy Environ. Sci.*, 2024, **17**, 2753–2764

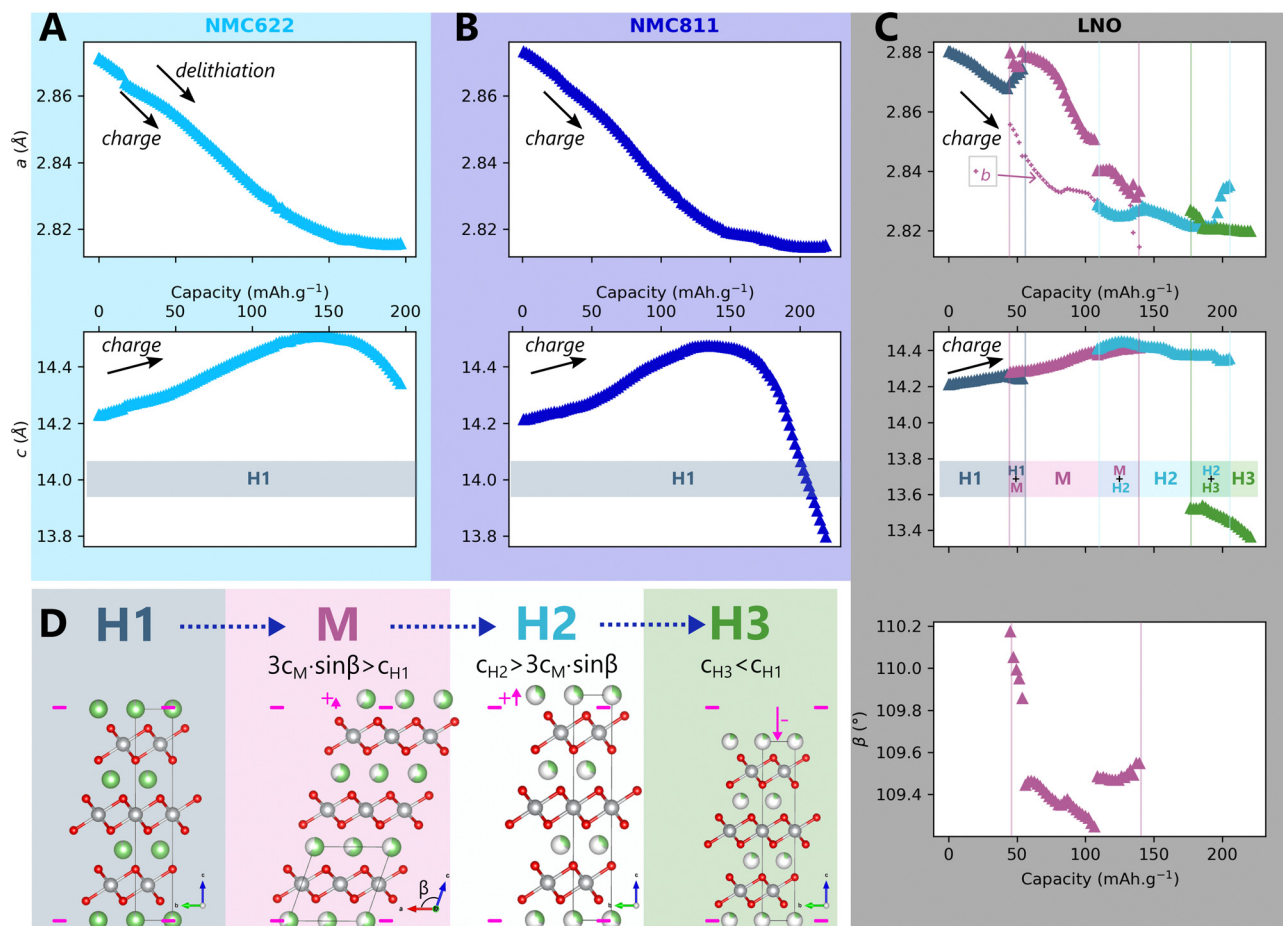This journal is © The Royal Society of Chemistry 2024

Fig. 3 Structural evolution of high nickel content layered oxides during cycling. Structural evolution at C/100 until 4.3 V *vs.* Li/Li$^+$ and phase diagram enclosed of (A) NMC622, (B) NMC811 and (C) LNO as a function of the capacity. $a/\sqrt{3}$ and b lattice parameter of the M phase are plotted for LNO. (D) The four refined phases of LNO during delithiation.

maximum value of $\frac{\mathrm{d}}{\mathrm{d}c_{Li}}(d_{TM})$ is found at a same lithium content, $c_{Li} \simeq 0.62$ (Fig. S13B, ESI†). The existence of the characteristic lithium contents is strengthened by both their existence in discharge (Fig. S13D, ESI†), and their existence when these materials are charged at C/100 (ESI† Section S10). Therefore, we suspect these features to be common to all NMC*xyz* with $x \geq 0.33$, as supported by simulations of Min *et al.*[37] Additionally, the position of the d_{IL} maximum is also in agreement with the mobility and hopping rates of lithium in NMC811 since both are decreasing from $c_{Li} \simeq 0.4$[13] from the moment the galleries gap height is reduced, hindering lithium diffusion.

The similarity of layered TM oxides is further supported by the NMC811 d_{IL} evolution above 4.2 V (Fig. S9, ESI†). d_{IL} in NMC811 tends toward that of LNO, though limited by its distinct chemical composition. Moreover, d_{TM} and d_{IL} in LNO evolve as in the other NMCs, even though it undergoes phase transformations, confirming their resemblance. Therefore within this frame, $X \simeq f(c_{Li})$, greatly simplifying the structure of NMC*xyz*.

3.5 Strain analysis

We now show that strain ε can also be described by a single variable c_{Li}. Peak broadening, as observed earlier at slow charge rate, can indicate a certain evolution of strain present in the structure during cycling. This strain could be either isotropic, meaning that the material is identically stressed in all directions in space, or anisotropic, when the strain develops in one particular direction of space. Generally, distinguishing isotropic from anisotropic strain in solid-state materials lies in a careful examination of the various hypothesis behind each potential cause and physical process. In the present case, isotropic strain analysis may be ambiguous, or even impractical, because of the possible confusion between heterogeneous lithiation state of particles and particles under stress, when assuming an isotropic space distribution. Because the strain represents a scale of heterogeneity of lattice parameters with respect to its averaged value, identical modifications of the XRD patterns would arise from an isotropic strain or a multi-alike-phases material, making impossible to differentiate the two situations (see ESI† Section S13). Here, we naturally face such burden, since heterogeneous lithiation states are intrinsic to polycrystalline NMCs.[26,27,38] Moreover, extended exposure of the material to the X-ray beam might artificially broaden the Bragg peaks, although the exposure has been limited in this work.[36] These two reasons prevent the analysis of isotropic strain to be properly performed. Alternatively, anisotropic
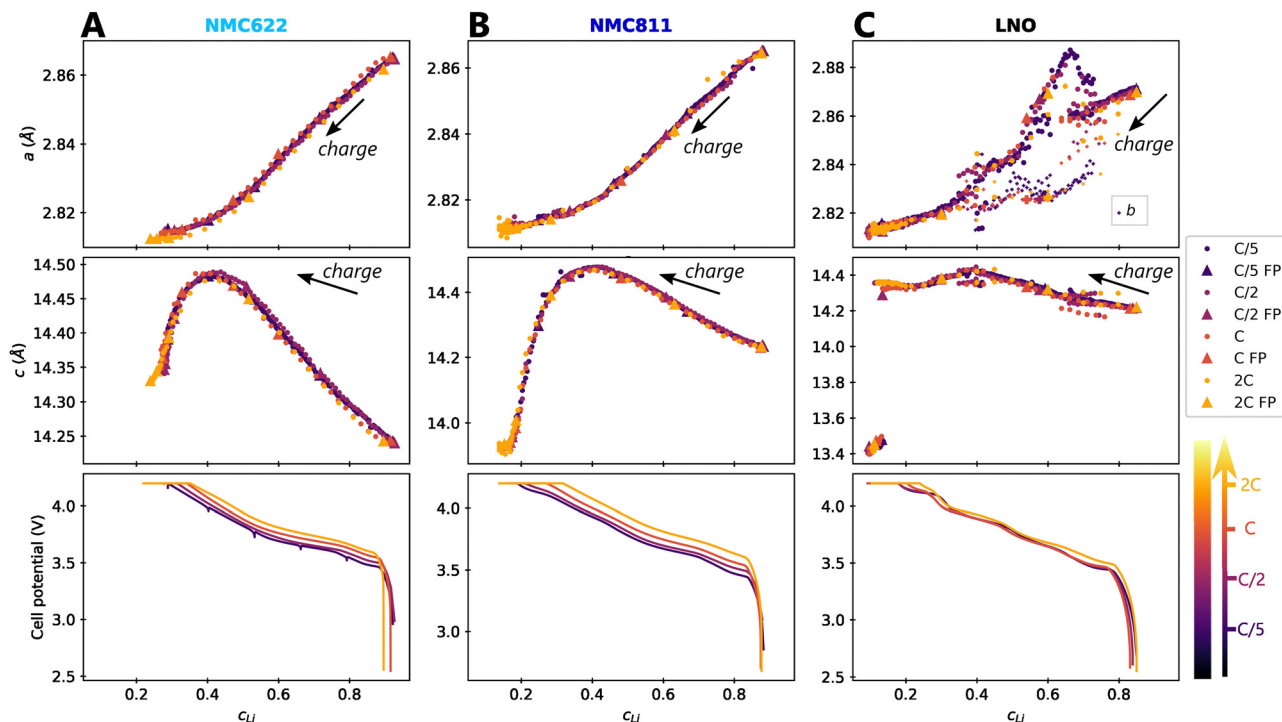
Fig. 4   Impact of C-rate on structural evolutions during cycling. Structural evolution and potential curves of (A) NMC622, (B) NMC811 and (C) LNO as a function of lithium content c_{Li} for increasing C-rates from darker to lighter colors. $a/\sqrt{3}$ and b lattice parameter of M phase are plotted for LNO, but its four phases are not distinguished. The potential spikes of the C/5 curve of NMC622 are rest periods and have no incidence on the present results. The label "FP" stands for parameters refined from the Full Pattern, accounting for every diffraction peaks. A part of refined parameters during the H2−H3 transition were removed due to a bias in the fit making the results less reliable. The full dataset is provided in Fig. S6 (ESI†).

strain analysis could be applied since it does not affect every diffraction peaks. In the specific case of NMC materials, however, while extracting the features of anisotropic strain using powder XRD data turned out to be possible, it appeared not possible to ascribe broadening effects to one or the other cause. In fact, as we now discuss in more details, local hererogeneities and anisotropic strain may be bound and both trigger the same aftereffects on the XRD patterns.

Firstly, let us discuss how lithiation heterogeneties can create anisotropic features in NMCs. Those are particularly insidious because they stem from a local heterogeneity of lithium concentration homogeneously distributed at the crystal scale. This lithium heterogeneity represents a heterogeneous lithium concentration within the galleries of a single crystal. This is not modelled by the $R\bar{3}m$ space group since the latter assumes a homogeneous distribution of the lithium in the layers. Due to the larger variation of the lattice parameter c compared to a, the crystalline concentration heterogeneity naturally induces anisotropic effects.

Let us consider f_a and f_c, two functions describing $a(c_{Li})$ and $c(c_{Li})$, obtained by smoothing the experimental results at C/5, as shown in Fig. 6A and B. The strain ε represents the heterogeneity of lattice parameters as compared to the equilibrium value, here simplified by the averaged value. Considering this, we can roughly estimate the endured strain along $\vec{a}$, ε^a associated with a local heterogeneity Δc_{Li}, of c_{Li}, according to

eqn (1):

$$\varepsilon^a(c_{Li}, \Delta c_{Li}) = \frac{|f_a(c_{Li} - \Delta c_{Li}/2) - f_a(c_{Li} + \Delta c_{Li}/2)|}{f_a(c_{Li})} \quad (1)$$

f_a is substituted by f_c in eqn (1) to calculate the strain along $\vec{c}$, ε^c, and both are plotted in Fig. 6C and D respectively, for various amplitude of Δc_{Li}. Therefore, eqn (1) gives strain as a function of two variables, c_{Li} and Δc_{Li}.

Although a weak strain is present in both $\vec{a}$ and $\vec{c}$ directions for c_{Li} in the range [0.4,1], its intensity decreases below $c_{Li} = 0.4$ along direction $\vec{a}$, while that along direction $\vec{c}$ increases until reaching a value about 30 times higher. This is typically reflecting the appearance of an anisotropic strain, since the strain is significantly more pronounced in a direction with respect to the other. These effects can be measured by XRD since the heterogeneity can be interpreted as lattice domains of the same crystal with distinct lattice parameters. Accordingly, the warping of the Bragg diffraction peaks caused by the lattice parameter evolution has been simulated and compared to the experimental data to validate the direct impact of local heterogeneities on the shape of diffraction peaks (ESI† Section S16 and Fig. S20). This analysis confirms the similar modification of both simulated and experimental Bragg peaks below $c_{Li} = 0.4$. It reveals that the local heterogeneity Δc_{Li} varies, and increases further below $c_{Li} = 0.4$. It suggests also that Δc_{Li} is a function of
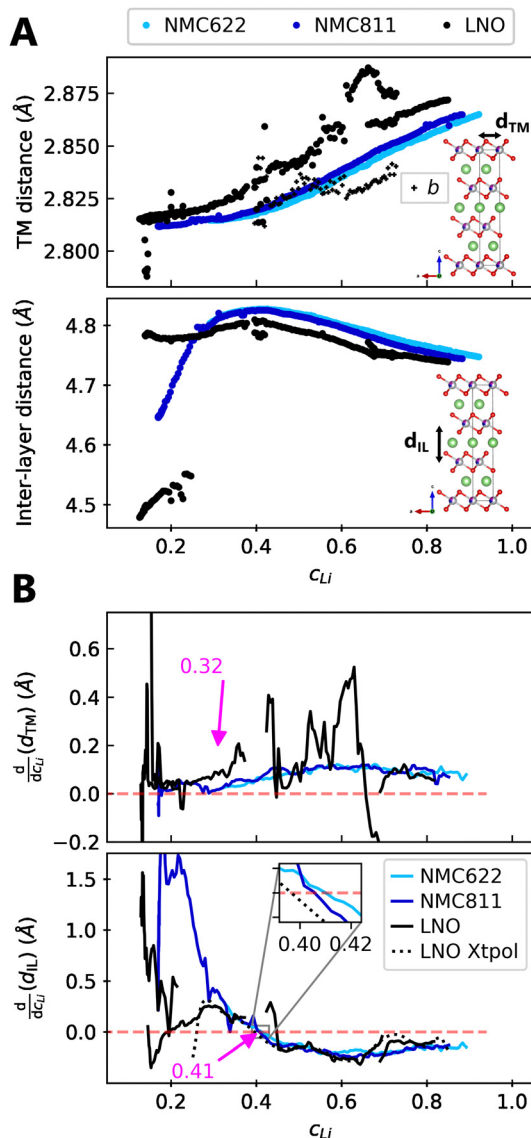
Fig. 5 Crystallographic distances evolutions in function of lithium concentration. (A) TM and inter-layer (IL) distances (respectively a and $c/3$ for hexagonal symmetry) from refined lattice parameters of NMC622, NMC811 and LNO charged at C/5 and measured by S-XRD. (B) Derivatives of centered rolling mean of d_{TM} and d_{IL} by lithium content c_{Li} for NMC622, NMC811 and LNO. The black dotted line is the derivative of the LNO interpolation curve of c parameter defined in Fig. S10 (ESI†). The red dashed line stands for the zero. The same trend is observed at C/100 in Fig. S3 (ESI†), although the calculation of c_{Li} is less reliable with the cell used at C/100.

c_{Li} only in early cycling, implying that ε is function of one variable only as shown later.

Secondly, now that the possible effect of local lithiation heterogeneities on local strain has been quantified, we refine the XRD data obtained across the various nickel content NMCs and at several charge rates, using anisotropic strain description. This second analysis method is based on the refinement of diffraction peaks distortion which proceeds from the lattice distance deviations. We observed a larger broadening of 003 compared to 101 Bragg reflection at the end of charge (Fig. S2 and S3D, ESI†). Other $\langle hkl \rangle$ reflections having larger l

component with respect to h and k have the same broadening at higher q values. This behaviour is typical of anisotropic strain oriented in the $\vec{c}$ direction, and is coherent with the large shrinkage of c in the NMCs and LNO. The unidirectionnal feature is confirmed by the anisotropic strain parameter obtained from Le Bail refinement at C/100 which is null at the beginning of charge and becomes positive at the same time for the three NMCs (Fig. S17, ESI†). For LNO, the anisotropy is correlated to the H3 phase only, and seems to be absent in the other phases, suggesting a special mechanism bound to H3.

The Le Bail refinement of anisotropic strain in the three materials at different cycling conditions in function of the lithium content is reported in Fig. 7. In this representation, all data point fall on a master curve with a specific exponential-growing trend at small c_{Li}. First of all, it means that faster kinetics does not induce stronger directional strain, since the anisotropic strain starts to increase from c_{Li} below 0.4–0.45 for the three materials, irrespective of the charge rate. Additionally, it indicates that the extent of anisotropic strain is not related to the material itself, but only to the amount of lithium filling the layers. It is unexpected to observe that neither the charge rate nor the NMC nickel stoichiometry impact the strain intensity, suggesting that its nature is exactly the same in the three layered TM oxides, independently of the crystalline structure. Furthermore, the anisotropic strain increases when NMC811 is overcharged until 4.65 V (blue star in Fig. 7). It confirms that the strain intensity is not related to the material itself, but only to the amount of lithium extracted, since its value tends toward that of LNO at a similar c_{Li}. Finally, a similar analysis during discharge shows that the anisotropic strain appears and vanishes at the same c_{Li} for the three materials during delithiation or lithiation (Fig. S18, ESI†). Thus, the anisotropic strain is reversible in layered TM oxides, at least in early cycles. It shows that strain depends only on c_{Li}, i.e. $\varepsilon = g(c_{Li})$, implying that either Δc_{Li} is not bound to ε, or that Δc_{Li} is directly bound to c_{Li}. That is why $\varepsilon = g(c_{Li}, \Delta c_{Li}) = g(c_{Li})$ in early cycling when the structure is still preserved.

The similarity of the strain estimated from local lithiation heterogeneities compared to what is experimentally obtained from XRD patterns refinements (Fig. 7 vs. Fig. 6D), is striking. Therefore, these results show that a local heterogeneity can induce effects that have the same consequences as an anisotropic strain created from other causes, such as from defects. It also suggests that strain is directly bound to the structure function f as given by eqn (1). Furthermore, whether the cause is anisotropic strain or a local lithiation heterogeneity, both strongly indicate a critical lithium content of 0.4 for Ni-rich layered TM oxides below which the structure is under exponential distortion from the very first cycles.

The existence of a critical lithium content reveals the underlying mechanism of layered TM oxides structures. Interestingly, the anisotropic strain appears when d_{IL} reaches its maximum (Fig. 5) and begins to decrease. Both shrinkage of the TM layers – which is still much debated in the community – and strain do appear in concert with a lithium depletion below $c_{Li} = 0.4$. Therefore, the two phenomena may find their cause in the
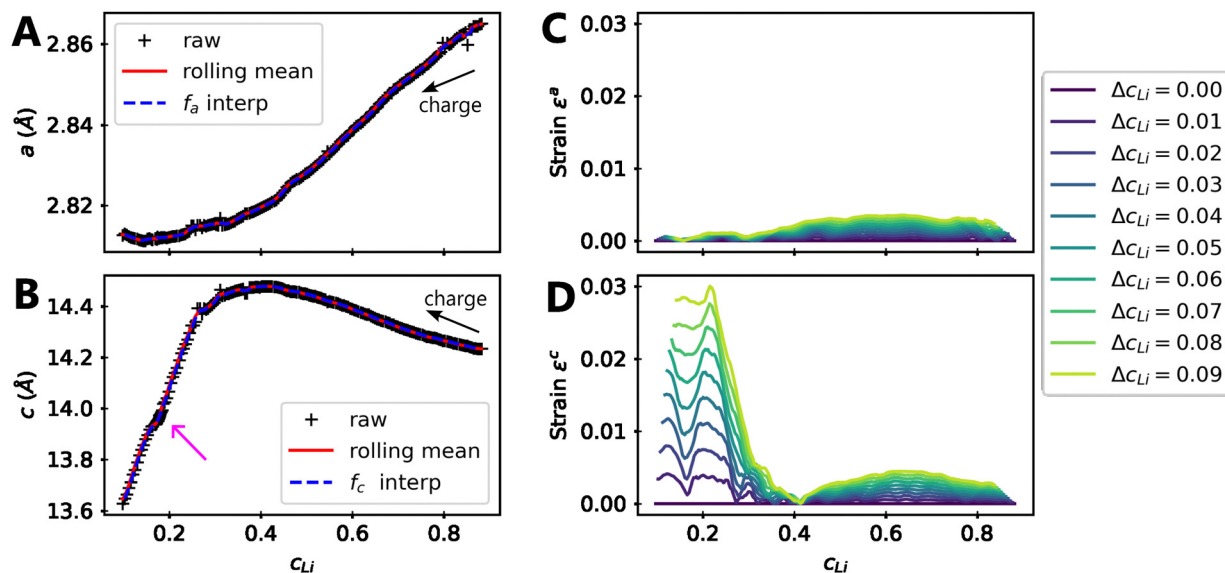
Fig. 6 Modelling of strain due to local heterogeneities. Refined (A) a and (B) c lattice parameters of NMC811 charged to 4.64 V in black markers, the rolling mean of the refined data in plain red, which is used to build the functions f_a and f_c in dashed blue. The magenta arrow indicates a constant voltage step at 4.2 V, before charging until 4.64 V. The strain is evaluated using eqn (1) along $\vec{a}$ direction in (C) and $\vec{c}$ in (D) for increasing local heterogeneities of c_{Li}, Δc_{Li}.
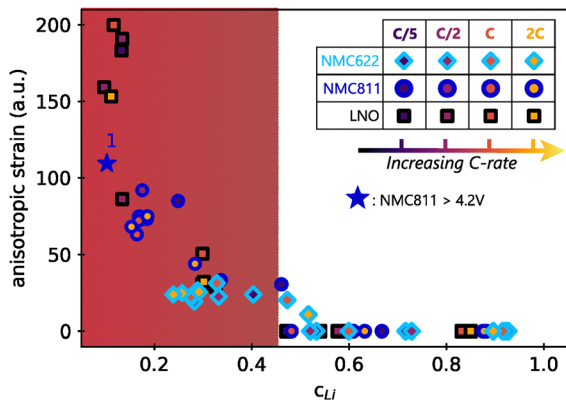

Fig. 7 Anisotropic strain in function of lithium content c_{Li}. Values were obtained by refining the full patterns with Le Bail method. The filling colors of markers indicate the charge rate associated with each of the three materials investigated. Same shape of markers are used for all LNO phases for better clarity. The blue star is the anisotropic strain of NMC811 during overcharge (see Fig. S9, ESI†). The anisotropic strain exponentially grows below a critical c_{Li} value ~ 0.4 (red zone).

same origin since they occur at the same time. Further investigation by X-ray absorption spectroscopy or by NMR may enable to clarify underlying mechanisms but are beyond the scope of this study. Importantly, the observation of a d_{IL} maximum can be seen in previously reported results in Ni-rich NCA (accompanied by cracks), LiCoO₂ and many sodiated layered TM oxides at a comparable c_{Li} or c_{Na}, *i.e.* 0.4 for most and 0.45 for LCO.[39–43] This suggests that such a lithium (and likely sodium) threshold exists in many layered TM oxides. Changing the chemical composition may shift the absolute value of the c_{Li} threshold, but not the very nature of the

structural mechanism. This model describes the structure as $X = f(c_{Li})$, and strain as $\varepsilon = g(c_{Li}, \Delta c_{Li})$ in the general case, and $\varepsilon = g(c_{Li})$ in early cycling. These common structure and strain features driven by the lithium content attest of a single mechanism shared by layered TM oxides.

3.6 Potential impact on degradation

The existence of anisotropic strain in the layered TM oxides could potentially favour stress-induced ageing of the materials. Strain creates stress as a function of the Young modulus, which in turn can lead to defects formation. In fact, Ni-rich layered TM oxides exhibit cracks induced by stress in primary and/or secondary particles, which are reported to be a major cause of degradation.[9,44] Since the strain describes lattice imperfections at the crystal level, it could favour crystalline cracks apparition. By crystalline cracks, here we intend cracks that nucleate and spread inside a single crystal, as opposed to those developed between primary particles of polycrystalline particles. Our results suggest that crystalline cracks are favoured below 40% lithium content in layered TM oxides, which corresponds to about 85% SOC for NMC622, but only 65% SOC for LNO. Previous studies reported cracks in single crystal NCA or NMC at high SOC,[3,10,45–47] the origin of which was often attributed to H2 → H3 transition or ageing. Based on the c_{Li}-driven master curve of strain, we infer that crystalline cracks appearance is instead correlated to very low lithium content, below the critical lithium value. Firstly, similar crystalline cracks also appear in NMC622 or NMC333 only when they are overcharged,[11,48,49] *i.e.*, when their lithium content is low. Secondly, crystalline cracks can be observed during the first cycles, which rules out a pure ageing effect but agrees with early developed strain-trigerred mechanism.[10,45,50]

Note that cracks at particle scale are different in nature from crystalline cracks. They are probably related to both volume changes[3,51] and inter-crystal strain[50,52] occuring at high SOC. The inter-crystal strain cannot be directly measured by XRD, but can be followed indirectly. A qualitative analysis based on our data (ESI† Section S17) suggests that the C-rate affects the inter-crystal strain only at high c_{Li}, when the solid lithium diffusion is low.[13,39,53,54]

In the literature, crystalline cracks are reportedly either nucleated from the surface or at edge dislocations within the crystal structure.[47,49] Both can be explained using the anisotropic strain evolution that we evidenced. Defects, such as Ni/Li antisites or stacking faults as described by the "crack incubation at dislocation core",[49] essentially distort the crystal along the $\vec{c}$ direction, hence inducing anisotropic strain. Those cracks are exacerbated by higher cutoff voltages, corroborating the increase of the anisotropic strain intensity when the lithium content is the lowest, such as the overcharged NMC811 in Fig. 6. Yet faster charge rates seem to provoke the appearance of crystalline cracks in some studies,[47,55] whereas our results support a crystalline strain independent of C-rate. It is likely due to the longer diffusion length of single crystals compared to the aggregated (but small) crystals of polycrystalline NMCs used in our study. Furthermore, larger heterogeneties are induced if the crystallographic orientation of the interface is not optimised[56,57] which favour crystalline cracks.[47,55] Therefore, it is possible that

crystalline cracks start to appear below $c_{Li} = 0.4$ in layered TM oxides, and are reversible as long as they are still in the "incubation" stage, before crack propagation.

We propose that local lithiation heterogeneities, anisotropic strain, defects present at the pristine state and crystalline cracks are actually closely bound to each other. Defects present before the first delithiation have been observed in NCA and $LiCoO_2$,[58,59] as well as defects appearing or spreading during the charge in a Ni-rich NMC or in a Li-rich layered oxide, respectively.[60,61] Those could alter the local equilibrium potential and as a consequence, the lithium pathway, which suggests that a mechano-chemical equilibrium potential drives the lithium insertion at very local scale, as proposed for $LiCoO_2$.[62] The mechano-chemical potential can favour local lithium concentration heterogeneities, which would induce a local warping of the lattice, and finally anisotropic strain. The distorted lattice could easily trigger crystalline cracks, that in turn affect the local mechano-chemical equilibrium potential. Thus, it is proposed that lithiation heterogeneities and anisotropic strain act in concert, and finally lead to the creation of crystalline cracks. Hence we suggest a single mechanism unifying both structure, local lithium distribution heterogeneities, strain and cracks at crystal scale in layered TM oxides. This mechanism is driven by the lithium content, irrespective of the nickel content, the charge rate, the phase diagram and likely of the poly/single crystalline nature (Fig. 8). When c_{Li} exceeds 0.4,
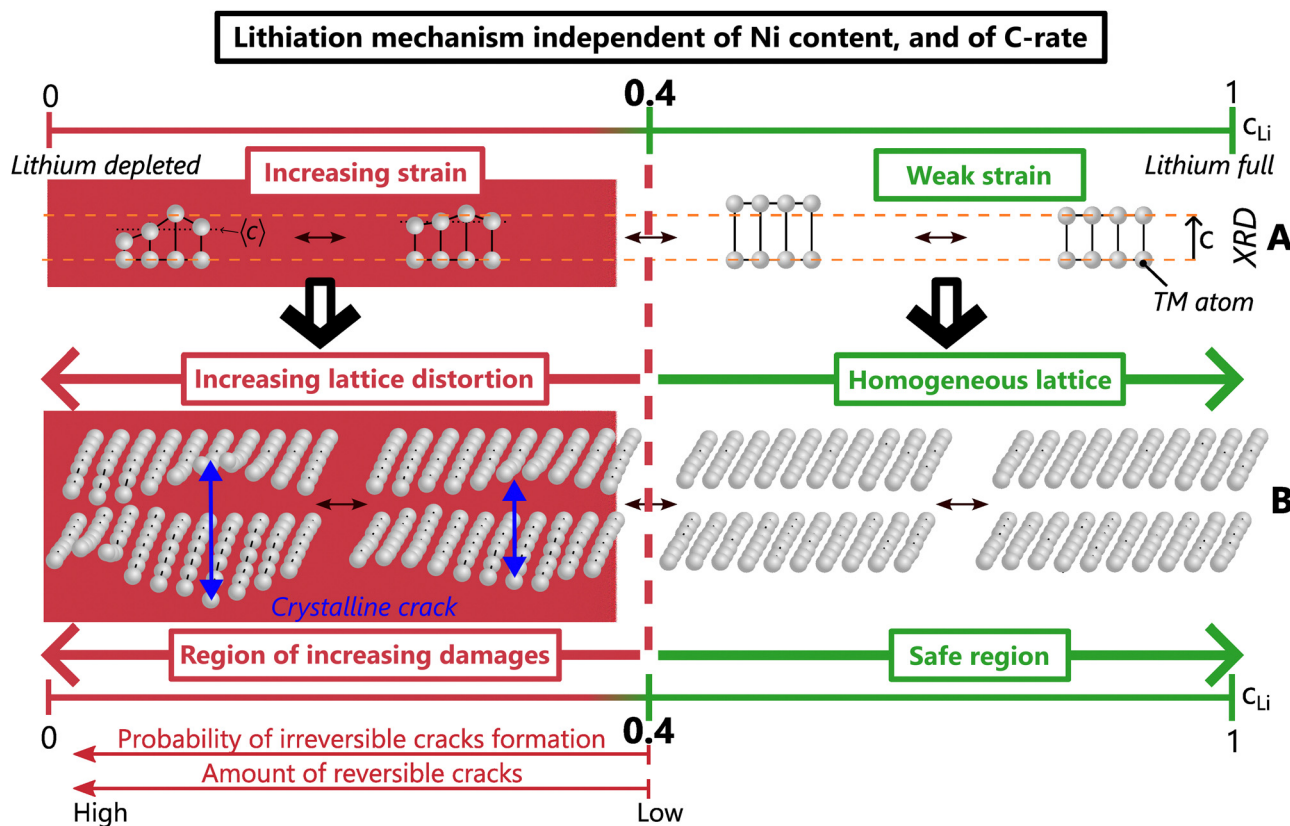

Fig. 8 Unified mechanism for structure, crystalline strain and cracks, in Ni-rich layered TM oxides driven by the lithium content c_{Li}. (A) Exaggerated evolution of 3 unit cells to picture lattice breathing and strain in $\vec{c}$ direction at low c_{Li}. (B) Schematic of TM layers distortion due to a reversible crack.

This journal is © The Royal Society of Chemistry 2024

Energy Environ. Sci., 2024, **17**, 2753–2764 | **2761**

weak strain and homogeneous lattice constitute the safe zone where crack nucleation is very unlikely. In contrast, below $c_{Li} = 0.4$, the increasing strain induces more and more lattice distortions, and a higher probability of forming crystalline cracks, that cause considerable damage to the material.

Our results highlight the key role of lithium loss in the layered TM oxides degradation not only because it limits the capacity of the battery, but also because it directly exacerbates material degradation. Due to lithium loss, the lithium content range in the positive active materials during operation is gradually shifting to lower values, further and further below the critical content. This shift intensifies the material strain and irreversible cracks, and consequently favours TM dissolution, oxygen leak or structure reconstruction into rocksalt or spinel type,[63] likely due to parasitic reactions with electrolyte at high voltage, further promoting lithium loss. Thereby, lithium loss turns into a vicious circle in which the greater the lithium loss, the larger the irreversible degradations, and reciprocally. In this regard, lithium loss could be considered as the dominant factor of degradation since it triggers many others. Its impact may be mitigated either by lithium regeneration, or by shifting to a lower c_{Li} value the critical content. The first could be realised with pre-formation of the solid electrolyte interphase which consumes a large amount of lithium. The second can be achieved by lattice doping or coating to stabilise the emptied layered structure, such as with Zr, Mo, Nb or other materials that showed increased capacity and less cracks appearance.[64,65] Other strategies exist to alleviate intergranular cracks at particle scale such as a protective surface layer, an optimised crystallographic orientation, or the building of a gradient of TM atoms inside secondary particles of layered TM oxides.[56,66–70]

4. Conclusions

In conclusion, combined laboratory and synchrotron *operando* structural studies of Ni-rich NMCs confirmed that phase transitions occur only in LNO, in contrast to the solid solution mechanism for NMC622 and NMC811 during the entire (de)lithiation. Nevertheless, by adopting a non-standard perspective to analyse the crystallographic data, we correlate the materials structure and degradation beyond the standard definition of phase transformation. LNO and NMCs show identical local structural and strain evolutions, which enables us to propose a unified model of the structure of layered TM oxides, irrespective of the nickel content, the charge rate, or the crystalline nature. This model is likely shared with many layered oxides. In this model, lithium extraction below a critical lithium content 0.4 triggers exponential lattice distortion, which is shown to be closely bound to the increase of anisotropic strain and local lithiation heterogeneities. Lithium loss is revealed as the main culprit in NMC fatigue by shifting the working window far below the critical content and triggers stress-induced parasitic reactions. As a consequence, battery manufacturers should envision to mark out the accessible

lithium content range depending on the layered TM oxide used, for example using potential derivatives (Fig. S24, ESI†), to preserve materials from degradation upon cycling.

Conflicts of interest

There are no conflicts to declare.

Acknowledgements

References

1 A. Manthiram, *ACS Cent. Sci.*, 2017, **3**, 1063–1069.

2 S. Li, Z. Jiang, J. Han, Z. Xu, C. Wang, H. Huang, C. Yu, S.-J. Lee, P. Pianetta, H. Ohldag, J. Qiu, J.-S. Lee, F. Lin, K. Zhao and Y. Liu, *Nat. Commun.*, 2020, **11**, 4433.

3 H.-H. Ryu, K.-J. Park, C. S. Yoon and Y.-K. Sun, *Chem. Mater.*, 2018, **30**, 1155–1163.

4 C. Xu, K. Märker, J. Lee, A. Mahadevegowda, P. J. Reeves, S. J. Day, M. F. Groh, S. P. Emge, C. Ducati, B. L. Mehdi, C. C. Tang and C. P. Grey, *Nat. Mater.*, 2021, **20**, 84–92.

5 Y. Mao, X. Wang, S. Xia, K. Zhang, C. Wei, S. Bak, Z. Shadike, X. Liu, Y. Yang, R. Xu, P. Pianetta, S. Ermon, E. Stavitski, K. Zhao, Z. Xu, F. Lin, X.-Q. Yang, E. Hu and Y. Liu, *Adv. Funct. Mater.*, 2019, **29**, 1900247.

6 K.-Y. Park, Y. Zhu, C. G. Torres-Castanedo, H. J. Jung, N. S. Luu, O. Kahvecioglu, Y. Yoo, J.-W. T. Seo, J. R. Downing, H.-D. Lim, M. J. Bedzyk, C. Wolverton and M. C. Hersam, *Adv. Mater.*, 2022, **34**, 2106402.

7 S. Zheng, C. Hong, X. Guan, Y. Xiang, X. Liu, G.-L. Xu, R. Liu, G. Zhong, F. Zheng, Y. Li, X. Zhang, Y. Ren, Z. Chen, K. Amine and Y. Yang, *J. Power Sources*, 2019, **412**, 336–343.

8 W.-S. Yoon, K. Y. Chung, J. McBreen and X.-Q. Yang, *Electrochem. Commun.*, 2006, **8**, 1257–1262.

9 C. D. Quilty, D. C. Bock, S. Yan, K. J. Takeuchi, E. S. Takeuchi and A. C. Marschilok, *J. Phys. Chem. C*, 2020, **124**, 8119–8128.

2762 | *Energy Environ. Sci.*, 2024, **17**, 2753–2764

This journal is © The Royal Society of Chemistry 2024

10 G. W. Nam, N.-Y. Park, K.-J. Park, J. Yang, J. Liu, C. S. Yoon and Y.-K. Sun, *ACS Energy Lett.*, 2019, **4**, 2995–3001.

11 G. Qian, Y. Zhang, L. Li, R. Zhang, J. Xu, Z. Cheng, S. Xie, H. Wang, Q. Rao, Y. He, Y. Shen, L. Chen, M. Tang and Z.-F. Ma, *Energy Storage Mater.*, 2020, **27**, 140–149.

12 S. Liu, P. J. West, H. Zhong, J. Bai, E. Stavitski, D. Leshchev, A. C. Marschilok, E. S. Takeuchi, D. C. Bock and K. J. Takeuchi, *Chem. Mater.*, 2023, **35**, 8857–8871.

13 K. Märker, P. J. Reeves, C. Xu, K. J. Griffith and C. P. Grey, *Chem. Mater.*, 2019, **31**, 2545–2554.

14 A. Jetybayeva, N. Schön, J. Oh, J. Kim, H. Kim, G. Park, Y.-G. Lee, R.-A. Eichel, K. Kleiner, F. Hausen and S. Hong, *ACS Appl. Energy Mater.*, 2022, **5**, 1731–1742.

15 J. Li, L. E. Downie, L. Ma, W. Qiu and J. R. Dahn, *J. Electrochem. Soc.*, 2015, **162**, A1401–A1408.

16 P.-Y. Liao, J.-G. Duh, J.-F. Lee and H.-S. Sheu, *Electrochim. Acta*, 2007, **53**, 1850–1857.

17 W. Li, H. Y. Asl, Q. Xie and A. Manthiram, *J. Am. Chem. Soc.*, 2019, **141**, 5097–5101.

18 O. J. Borkiewicz, K. M. Wiaderek, P. J. Chupas and K. W. Chapman, *J. Phys. Chem. Lett.*, 2015, **6**, 2081–2085.

19 Y. Zhang, L. Tao, C. Xie, D. Wang, Y. Zou, R. Chen, Y. Wang, C. Jia and S. Wang, *Adv. Mater.*, 2020, **32**, 1905923.

20 T. Danner, M. Singh, S. Hein, J. Kaiser, H. Hahn and A. Latz, *J. Power Sources*, 2016, **334**, 191–201.

21 T. Hirai, I. Yoshimatsu and J. Ichi Yamaki, *J. Electrochem. Soc.*, 1994, **141**, 611–614.

22 S. Tardif, N. Dufour, J.-F. Colin, G. Gébel, M. Burghammer, A. Johannes, S. Lyonnard and M. Chandesris, *J. Mater. Chem. A*, 2021, **9**, 4281–4290.

23 Y. Orikasa, T. Maeda, Y. Koyama, H. Murayama, K. Fukuda, H. Tanida, H. Arai, E. Matsubara, Y. Uchimoto and Z. Ogumi, *J. Am. Chem. Soc.*, 2013, **135**, 5497–5500.

24 X. Wu, B. Song, P.-H. Chien, S. M. Everett, K. Zhao, J. Liu and Z. Du, *Adv. Sci.*, 2021, **8**, 2102318.

25 Y.-N. Zhou, J.-L. Yue, E. Hu, H. Li, L. Gu, K.-W. Nam, S.-M. Bak, X. Yu, J. Liu, J. Bai, E. Dooryhee, Z.-W. Fu and X.-Q. Yang, *Adv. Energy Mater.*, 2016, **6**, 1600597.

26 J. Park, H. Zhao, S. D. Kang, K. Lim, C.-C. Chen, Y.-S. Yu, R. D. Braatz, D. A. Shapiro, J. Hong, M. F. Toney, M. Z. Bazant and W. C. Chueh, *Nat. Mater.*, 2021, **20**, 991–999.

27 W. E. Gent, Y. Li, S. Ahn, J. Lim, Y. Liu, A. M. Wise, C. B. Gopal, D. N. Mueller, R. Davis, J. N. Weker, J.-H. Park, S.-K. Doo and W. C. Chueh, *Adv. Mater.*, 2016, **28**, 6631–6638.

28 A. Vamvakeros, D. Matras, T. E. Ashton, A. A. Coelho, H. Dong, D. Bauer, Y. Odarchenko, S. W. T. Price, K. T. Butler, O. Gutowski, A.-C. Dippel, M. V. Zimmerman, J. A. Darr, S. D. M. Jacques and A. M. Beale, *Small Methods*, 2021, **5**, 2100512.

29 J. B. Leriche, S. Hamelet, J. Shu, M. Morcrette, C. Masquelier, G. Ouvrard, M. Zerrouki, P. Soudan, S. Belin, E. Elkaïm and F. Baudelet, *J. Electrochem. Soc.*, 2010, **157**, A606.

30 J. Rodríguez-Carvajal, *Phys. B*, 1993, **192**, 55–69.

31 J. Kieffer, V. Valls, N. Blanc and C. Hennig, *J. Synchrotron Radiat.*, 2020, **27**, 558–566.

32 V. Petrícek, M. Dušek and L. Palatinus, *Z. Kristallogr. - Cryst. Mater.*, 2014, **229**, 345–352.

33 H. Li, N. Zhang, J. Li and J. R. Dahn, *J. Electrochem. Soc.*, 2018, **165**, A2985–A2993.

34 L. De Biasi, A. Schiele, M. Roca-Ayats, G. Garcia, T. Brezesinski, P. Hartmann and J. Janek, *ChemSusChem*, 2019, **12**, 2240–2250.

35 H. Li, W. Hua, X. Liu-Théato, Q. Fu, M. Desmau, A. Missyul, M. Knapp, H. Ehrenberg and S. Indris, *Chem. Mater.*, 2021, **33**, 9546–9559.

36 T. Jousseaume, J.-F. Colin, M. Chandesris, S. Lyonnard and S. Tardif, *ACS Energy Lett.*, 2023, **8**, 3323–3329.

37 K. Min, K. Kim, C. Jung, S.-W. Seo, Y. Y. Song, H. S. Lee, J. Shin and E. Cho, *J. Power Sources*, 2016, **315**, 111–119.

38 L. Nowack, D. Grolimund, V. Samson, F. Marone and V. Wood, *Sci. Rep.*, 2016, 6.

39 A. Grenier, P. J. Reeves, H. Liu, I. D. Seymour, K. Märker, K. M. Wiaderek, P. J. Chupas, C. P. Grey and K. W. Chapman, *J. Am. Chem. Soc.*, 2020, **142**, 7001–7011.

40 H. Li, A. Liu, N. Zhang, Y. Wang, S. Yin, H. Wu and J. R. Dahn, *Chem. Mater.*, 2019, **31**, 7574–7583.

41 G. G. Amatucci, J. M. Tarascon and L. C. Klein, *J. Electrochem. Soc.*, 1996, **143**, 1114.

42 Y. Biecher, A. Baux, F. Fauth, C. Delmas, G. R. Goward and D. Carlier, *Chem. Mater.*, 2022, **34**, 6431–6439.

43 X. Li, Y. Wang, D. Wu, L. Liu, S.-H. Bo and G. Ceder, *Chem. Mater.*, 2016, **28**, 6575–6583.

44 C. Xu, P. J. Reeves, Q. Jacquet and C. P. Grey, *Adv. Energy Mater.*, 2021, **11**, 2003404.

45 J.-H. Kim, S. J. Kim, T. Yuk, J. Kim, C. S. Yoon and Y.-K. Sun, *ACS Energy Lett.*, 2018, **3**, 3002–3007.

46 A. K. C. Estandarte, J. Diao, A. V. Llewellyn, A. Jnawali, T. M. M. Heenan, S. R. Daemi, J. J. Bailey, S. Cipiccia, D. Batey, X. Shi, C. Rau, D. J. L. Brett, R. Jervis, I. K. Robinson and P. R. Shearing, *ACS Nano*, 2021, **15**, 1321–1330.

47 H.-H. Ryu, B. Namkoong, J.-H. Kim, I. Belharouak, C. S. Yoon and Y.-K. Sun, *ACS Energy Lett.*, 2021, **6**, 2726–2734.

48 P. Yan, J. Zheng, T. Chen, L. Luo, Y. Jiang, K. Wang, M. Sui, J.-G. Zhang, S. Zhang and C. Wang, *Nat. Commun.*, 2018, **9**, 2437.

49 P. Yan, J. Zheng, M. Gu, J. Xiao, J.-G. Zhang and C.-M. Wang, *Nat. Commun.*, 2017, **8**, 14101.

50 L. Romano Brandt, J.-J. Marie, T. Moxham, D. P. Förstermann, E. Salvati, C. Besnard, C. Papadaki, Z. Wang, P. G. Bruce and A. M. Korsunsky, *Energy Environ. Sci.*, 2020, **13**, 3556–3566.

51 A. O. Kondrakov, A. Schmidt, J. Xu, H. GeÃŸwein, R. Mönig, P. Hartmann, H. Sommer, T. Brezesinski and J. Janek, *J. Phys. Chem. C*, 2017, **121**, 3286–3294.

52 R. Xu and K. Zhao, *J. Mech. Phys. Solids*, 2018, **121**, 258–280.

53 V. Charbonneau, A. Lasia and G. Brisard, *J. Electroanal. Chem.*, 2020, **875**, 113944.

This journal is © The Royal Society of Chemistry 2024

Energy Environ. Sci., 2024, **17**, 2753–2764 | **2763**

54 S.-L. Wu, W. Zhang, X. Song, A. K. Shukla, G. Liu, V. Battaglia and V. Srinivasan, *J. Electrochem. Soc.*, 2012, **159**, A438.

55 Y. Bi, J. Tao, Y. Wu, L. Li, Y. Xu, E. Hu, B. Wu, J. Hu, C. Wang, J.-G. Zhang, Y. Qi and J. Xiao, *Science*, 2020, **370**, 1313–1317.

56 Z. Xu, Z. Jiang, C. Kuai, R. Xu, C. Qin, Y. Zhang, M. M. Rahman, C. Wei, D. Nordlund, C.-J. Sun, X. Xiao, X.-W. Du, K. Zhao, P. Yan, Y. Liu and F. Lin, *Nat. Commun.*, 2020, **11**, 83.

57 Y. Lu, T. Zhu, E. McShane, B. D. McCloskey and G. Chen, *Small*, 2022, **18**, 2105833.

58 S. Ahmed, A. Pokle, S. Schweidler, A. Beyer, M. Bianchini, F. Walther, A. Mazilkin, P. Hartmann, T. Brezesinski, J. Janek and K. Volz, *ACS Nano*, 2019, **13**, 10694–10704.

59 H. Gabrisch, R. Yazami and B. Fultz, *Electrochem. Solid-State Lett.*, 2002, **5**, A111.

60 S. Li, Z. Yao, J. Zheng, M. Fu, J. Cen, S. Hwang, H. Jin, A. Orlov, L. Gu, S. Wang, Z. Chen and D. Su, *Angew. Chem., Int. Ed.*, 2020, **59**, 22092–22099.

61 A. Singer, M. Zhang, S. Hy, D. Cela, C. Fang, T. A. Wynn, B. Qiu, Y. Xia, Z. Liu, A. Ulvestad, N. Hua, J. Wingert, H. Liu, M. Sprung, A. V. Zozulya, E. Maxey, R. Harder, Y. S. Meng and O. G. Shpyrko, *Nat. Energy*, 2018, **3**, 641–647.

62 Z. Xu, D. Hou, D. J. Kautz, W. Liu, R. Xu, X. Xiao and F. Lin, *Adv. Mater.*, 2020, **32**, 2003417.

63 H. Zhang, F. Omenya, P. Yan, L. Luo, M. S. Whittingham, C. Wang and G. Zhou, *ACS Energy Lett.*, 2017, **2**, 2607–2615.

64 F. A. Susai, D. Kovacheva, A. Chakraborty, T. Kravchuk, R. Ravikumar, M. Talianker, J. Grinblat, L. Burstein, Y. Kauffmann, D. T. Major, B. Markovsky and D. Aurbach, *ACS Appl. Energy Mater.*, 2019, **2**, 4521–4534.

65 F. Xin, A. Goel, X. Chen, H. Zhou, J. Bai, S. Liu, F. Wang, G. Zhou and M. S. Whittingham, *Chem. Mater.*, 2022, **34**, 7858–7866.

66 S. Tan, Z. Shadike, J. Li, X. Wang, Y. Yang, R. Lin, A. Cresce, J. Hu, A. Hunt, I. Waluyo, L. Ma, F. Monaco, P. Cloetens, J. Xiao, Y. Liu, X.-Q. Yang, K. Xu and E. Hu, *Nat. Energy*, 2022, **7**, 484–494.

67 D. Ren, E. Padgett, Y. Yang, L. Shen, Y. Shen, B. D. A. Levin, Y. Yu, F. J. DiSalvo, D. A. Muller and H. D. Abruña, *ACS Appl. Mater. Interfaces*, 2019, **11**, 41178–41187.

68 S. Natarajan, S. B. Moodakare, P. Haridoss and R. Gopalan, *ACS Appl. Mater. Interfaces*, 2020, **12**, 34959–34970.

69 K.-J. Park, M.-J. Choi, F. Maglia, S.-J. Kim, K.-H. Kim, C. S. Yoon and Y.-K. Sun, *Adv. Energy Mater.*, 2018, **8**, 1703612.

70 C. S. Yoon, K.-J. Park, U.-H. Kim, K. H. Kang, H.-H. Ryu and Y.-K. Sun, *Chem. Mater.*, 2017, **29**, 10436–10445.

2764 | *Energy Environ. Sci.*, 2024, **17**, 2753–2764

This journal is © The Royal Society of Chemistry 2024